ISSN 1808-8546 (ONLINE) 1808-3765 (CD-ROM)

ESTIMATIVA DO SALDO DE RADIAÇÃO DO AÇAÍ IRRIGADO POR MEIO DE SENSORIAMENTO REMOTO NO LESTE DA AMAZÔNIA

EWELYN REGINA ROCHA SILVA [1]; DENILSON BARRETO DA LUZ[2]; DENIS DE PINHO SOUSA[3]; LUCAS BELÉM TAVARES[4]; BERNARDO BARBOSA DA SILVA[5] E PAULO JORGE DE OLIVEIRA PONTE DE SOUZA[6]

[1] Mestre em Agronomia pelo programa de Pós-Graduação em Agronomia – PgAgro, Universidade Federal Rural da Amazônia, Av. Presidente Tancredo Neve, 2501, Terra Firme, 66077-830, Belém, Pará, Brasil, ewelynrocha@gmail.com.
[2] Graduando em Agronomia, Laboratório de Agrometeorologia, Universidade Federal Rural da Amazônia, Av. Presidente Tancredo Neve, 2501, Terra Firme, 66077-830, Belém, Pará, Brasil, denilsong97@gmail.com.
[3] Engenheiro Agrônomo, Doutor em Agronomia, Fiscal de Meio Ambiente na Secretaria de Estado de Meio Ambiente e Sustentabilidade do Pará, Rua do Utinga, n° 717, bairro Curió Utinga, CEP: 66610-010, Belém, PA, Brasil, denisdepinho@agronomo.eng.br.
[4] Mestrando no programa de Pós-Graduação em Ciências Florestais, Universidade Federal Rural da Amazônia, Av. Presidente Tancredo Neve, 2501, Terra Firme, 66077-830, Belém, Pará, Brasil, lucas.belem.tavares@gmail.com.
[5] Centro de Tecnologia e Recursos Naturais, Universidade Federal de Campina Grande, Rua Aprígio Veloso, 882, Campina Grande, 58429-900, Campina Grande, Paraíba, Brasil, bernardo.silva@ufcg.edu.br.
[6] Instituto Socioambiental e dos Recursos Hídricos, Laboratório de Agrometeorologia, professor no programa de Pós-Graduação em Agronomia, Universidade Federal Rural da Amazônia, Av. Presidente Tancredo Neve, 2501, Terra Firme, 66077-830, Belém, Pará, Brasil, paulo.jorge@ufra.edu.br.

1 RESUMO

Muitas áreas na Amazônia foram modificadas, alterando as trocas energéticas neste ambiente. Essa mudança é uma das responsáveis pelas variações no saldo de radiação (R_n), pois afetam a troca de energia entre a superfície e a atmosfera. O objetivo foi estimar o R_n em uma área de açaí irrigado na Amazônia Oriental. Foram utilizadas imagens do satélite Landsat 8, do dia sequencial do ano (DAS) 151/2018 e DAS 241/2019, referente às órbitas/pontos 222/61 e 223/61, respectivamente. O R_n foi obtido por meio do algoritmo *Surface Energy Balance Algorithm for Land* – SEBAL, que se fundamenta na radiância dos canais reflexivos e termal do sensor. Os resultados (sensor x superfície) mostraram-se satisfatórios com valores de erro absoluto médio (EAM) iguais a 4,92 W/m^2 e 15,66 W/m^2, erro relativo médio (ERM) iguais a 0,98 % e 3,4 % para DAS 151 e o DAS 241, respectivamente. Observou-se a capacidade do SEBAL em diferenciar tipos de coberturas do solo, o que proporcionou elaborar a distribuição espacial do Rn na cena analisada e no plantio de açaí, demostrando assim, a sensibilidade do modelo e a importância da variabilidade espacial existente na área, essas informações podem auxiliar as tomadas de decisões quanto ao manejo de irrigação.

Keywords: sebal, variabilidade espacial, landsat 8.

SILVA, E. R. R.; LUZ, D. B.; SOUSA; D. P.; TAVARES, L.B. SILVA, B. B.; SOUZA, P. J. O. P.
ESTIMATION OF THE RADIATION BALANCE OF IRRIGATED AÇAÍ THROUGH REMOTE SENSING IN EAST AMAZONIA

Recebido em 25/01/2021 e aprovado para publicação em 03/11/2021
DOI: http://dx.doi.org/10.15809/irriga.2021v26n3p664-683

2 ABSTRACT

Many areas in the Amazon have been modified, altering the energy exchanges in this environment. This change is a factor responsible for variations in the radiation balance (R_n), as they affect the energy exchange between the surface and the atmosphere. The objective was to estimate the R_n in an açaí irrigated area in Eastern Amazon. Landsat 8 satellite images of the sequential day of the year (DAS) 151/2018 and DAS 241/2019, referring to orbits/points: 222/61 and 223/61, respectively, were used. The R_n was obtained through the Surface Energy Balance Algorithm for Land - SEBAL algorithm, which is based on the radiance of the reflective and thermal bands of the sensor. The results (sensor x surface) were satisfactory with mean absolute error (EAM) values equal to 4.92 W/m^2 and 15.66 W/m^2, mean relative error (ERM) equal to 0.98% and 3.4% for DAS 151 and DAS 241, respectively. SEBAL's ability to differentiate types of land cover was observed, which provided the elaboration of the spatial distribution of Rn in the analyzed scene and in the açaí planting, so demonstrating the sensitivity of the model and the importance of spatial variability in the area, this information can help in decision-making regarding irrigation management.

Keywords: sebal, spatial variability, landsat 8.

3 INTRODUCTION

The radiation balance (R_n) is the sum of shortwave and longwave radiation, and its estimation is essential for the study of soil–vegetation–atmosphere interactions in the fields of agronomy, soil science, environmental engineering, geotechnical engineering, and other areas (AN; HEMMATI; CUI, 2017). Changes in land use and occupation and precipitation are some of the main factors responsible for variations in R_n, as they affect the exchange of energy and mass between the surface and the atmosphere (ENORÉ, 2012). With agricultural intensification in the Brazilian Amazon since the 1990s, many areas have been modified (MACEDO *et al*., 2012), consequently altering energy exchanges in this environment.

influences Earth's climate and weather conditions. The Rn available at the surface is obtained from solar radiation that reaches the ground and is divided into energy for heating the air (H) and the soil (G) and for evaporative processes of the plant (λET), and the partition of this energy is driven by the type and state of the surface (ARAÚJO *et al*., 2021). The energy balance of vegetated surfaces allows estimation of mass and energy exchanges in the soil–plant–atmosphere system by studying the partitioning of Rn in the various processes that occur in the crop, which allows the evaluation of changes in the vegetation microclimate depending on the crop development stages and soil and atmospheric conditions, and this can assist in decision-making regarding crop management, including irrigation (FONTANA; BERLATO; BERGAMASCHI, 1991).

The Rn can be measured punctually via sensors designed for reading, such as balance radiometers, or by measuring its components via pyranometers. This is the most accurate way to quantify incident solar radiation on the surface (SOUZA; ESCOBEDO, 2013). However, the reading performed through these sensors is limited to small areas because of their punctual nature of data reading (MACHADO *et al*., 2014). Therefore, owing to the diversity of the surface, these measurements cannot be directly extrapolated to regional scales

(BASTIAANSSEN *et al*., 2005) since they are not representative of larger areas.

One possibility for overcoming the limitations of these point measurements is to use remote sensing (RS) data to estimate, among other variables, Rn. In recent decades, the provision of orbital images from RSs has been an important tool for estimating the components of the energy balance, enabling observation of the spatiotemporal behavior of the radiation balance at different locations and times of the year. Among the various existing models for this purpose, the *surface energy balance algorithm for land* (SEBAL), proposed by Bastiaanssen in 1995, stands out. It estimates the components of the energy balance via thermal and multispectral images and a few auxiliary meteorological data (BASTIAANSSEN *et al*., 1998).

Since then, the SEBAL model has been used in several biomes and different analyses around the world, obtaining satisfactory results according to the conclusions of Santos *et al*. (2014), who studied Rn $_{in}$ pasture and forest areas in the Amazon in the dry season; Pavão *et al*. (2017), whose objective was to evaluate the impacts of deforestation on biophysical variables in the municipality of Apuí-AM; Alves *et al*. (2017), who obtained estimates of the net radiation at the surface of the Pajeú River basin through Landsat-8 images; Debastiani *et al*. (2018), who achieved the objective of estimating Rn through remote sensing techniques, compared it with data estimates from a surface station in São Joaquim National Park for January 30, 2014, and studies by Veloso, Silva and Ferreira (2020), who analyzed Rn in vereda areas in northern Minas Gerais in the Cerrado biome.

On the basis of combinations of empirical relationships and physical parameterizations, the algorithm enables the calculation of surface fluxes for areas with different land covers and the calculation of the radiation balance and energy balance components for each image pixel (ALLEN; TASUMI; TREZZA, 2002; BASTIAANSSEN *et al*., 1998), without the need for extensive field measurements. Therefore, comparative studies between data estimated from orbital images and data collected in the field are important since the advent of numerical modeling could be an effective tool for addressing the lack of observations of meteorological variables in remote areas (PINTO *et al*., 2010).

The present work aimed to estimate the radiation balance at the time of satellite passage in the eastern Amazon in an irrigated area cultivated with açaí (*Euterpe oleraceae* M.) via the SEBAL algorithm.

4 MATERIALS AND METHODS

4.1 Study area and dataset used

An açai plantation for commercial purposes has been located at Fazenda Ornela since 2012.

Figure 1 shows the study area and the micrometeorological tower in the açai plantation.

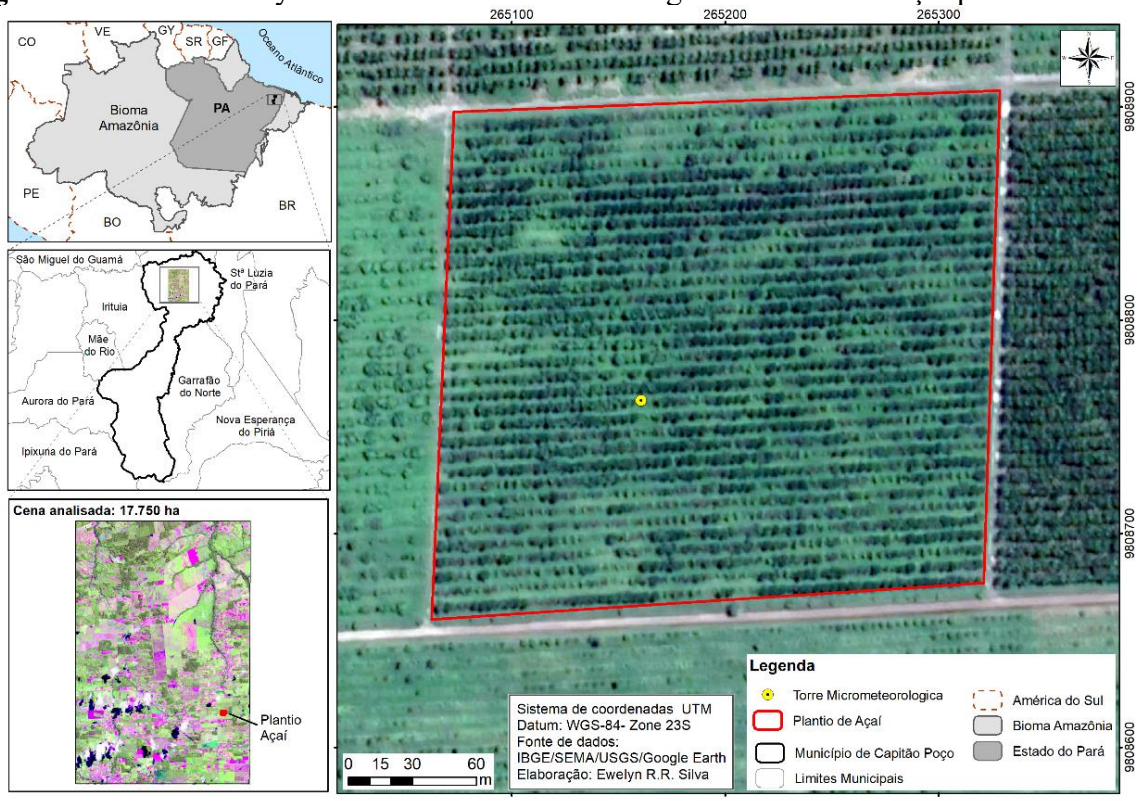

Source: Authors (2021).

According to the Köppen climate classification, the region's climate is characterized as Am (humid and subhumid tropical climates), with an average annual temperature of 25 °C and an average rainfall of 2,250 mm per year (ALVARES *et al*., 2013; RODRIGUES *et al*., 2016). The field experiment was implemented on 1 hectare of the plantation (Figure 1), with a spacing of 6.0 × 4.0 m, with three plants per clump, cultivated on dry land with daily irrigation during the driest four-month period of the year (August--November) via a microsprinkler system, through which a gross empirical depth of 3.28 mm was applied daily. This experiment was conducted during two açai harvests: the first between September 2017 (DAS 245) and October 2018 (DAS 303) and the second from November 2018 (DAS 305) to October 2019 (DAS 303). Data on meteorological variables (air temperature, relative humidity, wind speed and direction, net radiation, etc.) were obtained.

A micrometeorological tower was installed in the experimental area (Figure 1), where three automatic meteorological data loggers (*data loggers)* were attached and distributed along the canopy (two from Campbell Scientific, model CR1000, and one from Onset Hobo, model U30). The system program included sensor readings every ten seconds, with averages every 20 minutes. The tower location met the minimum area boundary requirements, with an available *fetch ratio* (greater than 1:100) so that the measurements obtained were representative of the experimental area without the influence of advective energy (RANA; KATERJI, 2000). Table 1 shows the sensors used in the experiment and their arrangement in relation to the ground or canopy. The data from the tower were compared with the net radiation data estimated with the SEBAL algorithm.

Table 1. Variables and instruments used in the experiment, as well as their arrangement in relation to the soil and plant canopy.

Meteorological variables	Instrument, manufacturer, model	Ground layout (m)
Air temperature	*Vaisala thermohygrometer* (HMP35A)	2.0 and 8.0 above ground
Relative humidity Air temperature Relative humidity	*Vaisala thermohygrometer* (HMP35A) *Hobo* (STHB-M002) *Hobo* (STHB-M002)	2.0 and 8.0 above ground 0.5 and 2.0 above the canopy 0.5 and 2.0 above the canopy
Soil moisture Rain	*Time Domain Reflectometer* (CS615) *Rain gauge* (TB4-L)	- 0.3 of the soil surface 0.5 above the canopy
Incident global radiation	*Pyranometer* (CMP6-L)	2.0 above canopy
Radiation balance	*Net Radiometer* (NR-LITE2-L)	2.0 above canopy

Source: Denis de Pinho Sousa (2020).

Two images generated by the *Operational Land* Imager—OLI and *Thermal Infrared Sensor* (TIRS) of the Landsat 8 satellite—were used; these images were acquired free of charge from the United States Geological Survey website (earthexplorer.usgs.gov). To select the days, the images were selected considering the least possible cloud interference in the study area, especially at the location of the micrometeorological tower and the tower's data collection period (referring to the years 2018 and 2019). Thus, an image was obtained from May 31, 2018 (orbit/point 222/61), Julian day (DAS) 151 (Figure 2a), and an image from August 29, 2019 (orbital/point 223/61), DAS 241 (Figure 2b).

Figure 2 Scenes analyzed in the study. (a) May 31, 2018, and (b) August 29, 2019**.**

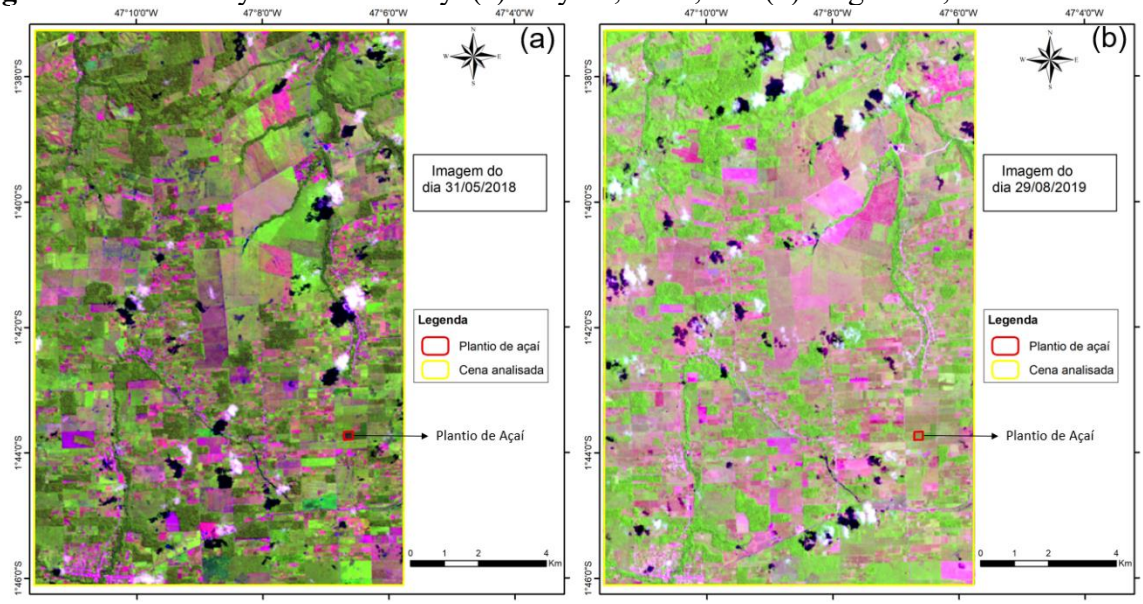

Source: Authors (2021).

To obtain the radiation balance, the SEBAL algorithm methodology was followed, which uses a combination of data generated from orbital satellite images and point data from meteorological stations. The radiation balance accounts for the downward and upward radiative fluxes, both shortwave and longwave, that interact with the Earth's surface (SILVA; BRAGA; BRAGA, 2011). The diagram below illustrates the steps taken to obtain Rn (Figure 3).

Figure 3 Computational steps to obtain the surface radiation balance via the SEBAL algorithm.

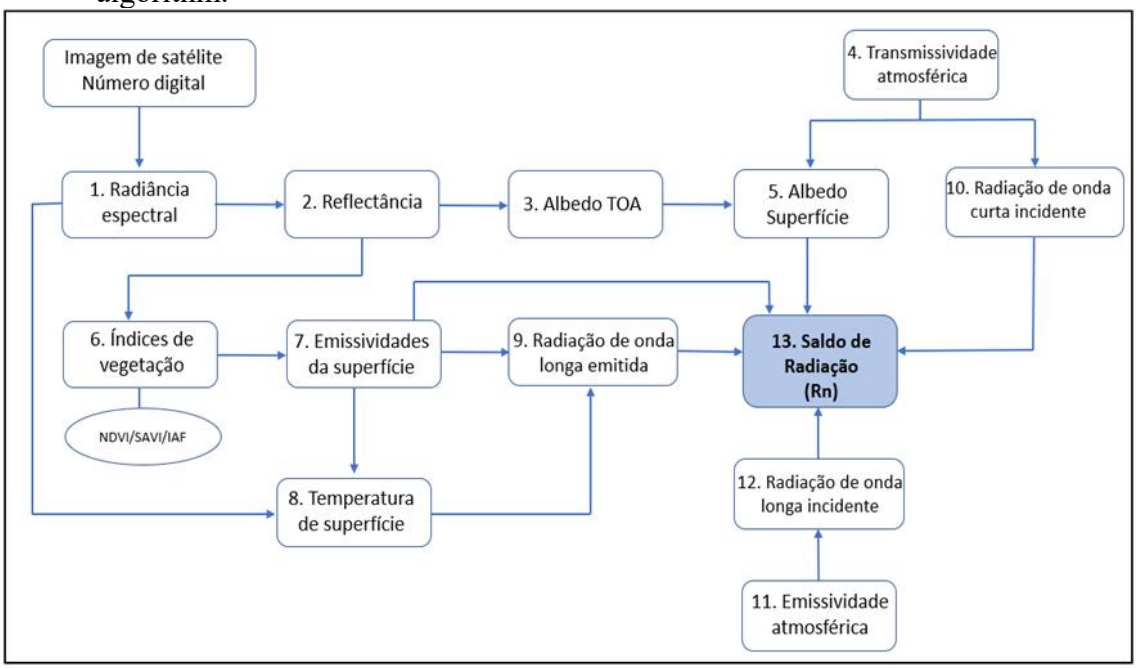

Source: Adapted from Allen, Tassumi and Trezza (2002).

The net radiation at the surface (R_n) (W m $^{-2}$), computed for the moment of the satellite's passage, was estimated according to Equation 1 (BASTIAANSSEN *et al* ., 1998) :

$$R_n = R_{sol,inc}\left(1 - \alpha_{sup}\right) - R_{ol,emit} + R_{ol,atm} - (1 - \varepsilon_0)\, R_{ol,atm} \quad (1)$$

where m represents $R_{sol,inc}$the incident shortwave radiation, α_{sup} represents the corrected albedo of each pixel, $R_{ol,atm}$ represents the longwave radiation emitted by the atmosphere, $R_{ol,emit}$ represents the longwave radiation emitted by the surface, and ε_0 represents the emissivity of each pixel.

The calculation of the planetary albedo (α_{toa}) was obtained via the linear combination of the monochromatic ρ'reflectances () of each of the reflective bands of the OLI sensor according to Equation 2 (TASUMI; ALLEN; TREZZA, 2008):

$$\alpha_{toa} = (\varpi_2 \rho'_2) + (\varpi_3 \rho'_3) + (\varpi_4 \rho'_4) + (\varpi_5 \rho'_5) + (\varpi_6 \rho'_6) + (\varpi_7 \rho'_7) \quad (2)$$

Each weight (ϖ) is obtained by the ratio between the band-specific solar constant b and the sum of all the constants $ESUN_{\lambda,b}$ according to Equation 3 (STARKS *et al*., 1991):

$$\varpi_{\lambda,x} = \frac{ESUN_{\lambda,b}}{\Sigma ESUN_{\lambda,b}} \quad (3)$$

For Landsat-8, the values are shown in Table 2.

Table 2. Weight coefficient (ϖ) for calculating the planetary albedo.

Bands	**B2**	**B3**	**B4**	**B5**	**B6**	**B7**
$\boldsymbol{\varpi_n}$	0.300	0.277	0.233	0.143	0.036	0.012
$\boldsymbol{ESUN_{\lambda,b}}$	2011.3	1853	1532.8	956.4	237.8	80.2

Source: Silva *et al*. (2016).

The monochromatic reflectance of each band (λi) (Equation (4)) was obtained from the ratio between the flux of reflected solar radiation and the flux of incident solar radiation (SILVA *et al* ., 2016) :

$$\rho_{\lambda i} = \frac{add_{ref,i} + Mult_{ref,i}.ND_i}{\cos Z.dr} \quad (4)$$

To determine the monochromatic spectral $L_{\lambda i}$radiance (Equation 5), the additive and multiplicative terms of the radiance group obtained from the image metadata were used:

$$L_{\lambda i} = add_{rad,i} + Mult_{rad,i}\,.\,ND_i \quad (5)$$

where for Equations (4) and (5), i corresponds to each band (2, 3, 4, 5, 6 and 7) of the image; $\rho\lambda$ represents the monochromatic reflectance; $add_{ref}\ e\ Mult_{ref}$ represents the additive and multiplicative terms of the reflectance of bands 2, 3, 4, 5, 6 and 7 (extracted from the metadata of each image); dr represents the correction for the eccentricity of the Earth's orbit; L_λ represents the monochromatic spectral radiance; and $add_{rad}\ e\ Mult_{rad}$ represents the additive and multiplicative terms of the thermal band NDradiance, which is the digital number of each pixel.

The surface albedo for each pixel, or the albedo corrected for atmospheric effects

(α) (Equation 6), was calculated on the basis of the model developed by Zhong and Li (1988) , which has been widely used (ALLEN; TASUMI; TREZZA , 2007 ; BASTIAANSSEN *et al* ., 1998, 2005; SILVA; BRAGA; BRAGA, 2011) :

$$\alpha_{sup} = \frac{\alpha_{toa} - \alpha_p}{\tau_{sw}^2} \quad (6)$$

where α_{toa} represents the albedo of each pixel without atmospheric correction, which combines the spectral reflectance values for all shortwave bands; α_p represents the atmospheric reflectance, which is considered in this study equal to 0.03 (ALLEN; TASUMI; TREZZA, 2007; BASTIAANSSEN *et al* ., 2005; SILVA; BRAGA; BRAGA, 2011) ; and τ_{sw} represents the atmospheric transmissivity, which depends on the solar zenith angle (*Z*), the atmospheric turbidity coefficient (*kt*), the atmospheric pressure (*P*) (kPa) and the amount of precipitable water (*W*) (mm), according to Equation 7 (ALLEN; TASUMI; TREZZA , 2007) :

$$\tau_{sw} = 0{,}35 + 0{,}627 \exp\left[\frac{-0{,}00146\,P}{K_t \cos Z} - 0{,}075\left(\frac{W}{\cos Z}\right)^{0{,}4}\right] \quad (7)$$

where *W* was calculated according to Equation 8 (GARRISON; ADLER, 1990) :

$$W = 0{,}14\, e_a \left(\frac{P}{P_o}\right) + 2{,}1 \quad (8)$$

where e_a represents the saturation vapor pressure (kPa), *P* represents the atmospheric pressure (hPa), and Po represents the atmospheric pressure at sea level (hPa).

The incident shortwave radiation $Rs_{sol,inc}$(W m $^{-2}$) (Equation 9) in the study area was determined by the parameterization scheme developed by Allen, Tasumi and Trezza (2007) :

$$Rs_{sol,inc} = S_o \cos Z\, dr\, \tau_{sw} \quad (9)$$

where S_o is the solar constant (1367 Wm $^{-2}$) and τsw is the atmospheric transmissivity obtained via Equation 7.

The longwave radiation emitted by the surface ($R_{ol,emit}$) (W m $^{-2}$) (Equation 10) was calculated via the Stefan–Boltzmann law:

$$R_{ol,emit} = \varepsilon_0 \sigma T_s^4 \quad (10)$$

where T_s represents the surface temperature in Kelvin; ε_0 represents the emissivity of each pixel; and σ represents the Stefan–Boltzmann constant (σ = 5.67. 10 $^{-8}$ W m $^{-2}$ K $^{-4}$).

The surface temperature (K) was calculated via the radiance and emissivity in the thermal band spectral domain (ε_{NB}) via Equation 11:

$$T_S = \frac{K_2}{\ln\left(\frac{\varepsilon_{NB} \cdot K_1}{L_{\lambda,10} - 0{,}29} + 1\right)} \quad (11)$$

where K $_1$ = 774.89 W m $^{-2}$ sr $^{-1}$ μm $^{-1}$ and K $_2$ = 1321.08 W m $^{-2}$ sr $^{-1}$ μm $^{-1;}$ the K terms correspond to the first and second radiation constants of band 10 (obtained from the image metadata);$L_{\lambda,10}$ is the spectral radiance of the thermal band; and 0.29 Wm $^{-2}$ sr $^{-1}$ μm $^{-1}$ is the calibration coefficient of the monochromatic spectral radiance.

The emissivities ε_{NB} and ε_0 were estimated on the basis of the parameterization obtained as a function of the leaf area index (LAI) (Equations (12) and

(13)) (ALLEN; TASUMI; TREZZA, 2007) :

$$\varepsilon_{NB} = 0{,}97 + 0{,}0033\,.\,IAF \quad (12)$$

$$\varepsilon_0 = 0{,}95 + 0{,}011\,.\,IAF \quad (13)$$

Information on the vegetation indices (IAF, SAVI and NDVI) was obtained as follows:

The leaf area index (LAI) was computed via the empirical equation obtained by Allen *et al*. (2002) according to Equation (14):

$$IAF = -\frac{\ln\left(\frac{0{,}69-SAVI}{0{,}59}\right)}{0{,}91} \quad (14)$$

The vegetation index adjusted for soil effects, i.e., the soil adjusted vegetation index (SAVI), was obtained according to Equation (15):

$$SAVI = \frac{(1+L).(r_4-r_5)}{(L+r_4+r_5)} \quad (15)$$

where L is a soil parameter, considered in this study as L = 0.5, used for intermediate vegetation densities (HUETE , 1988) and where r_4 and r_5 are the solar spectral reflectances corresponding to the near infrared (band 5) and red (band 4) regions, respectively.

The normalized difference vegetation index difference vegetation index (NDVI) was obtained according to Equation (16) described by Rouse *et al* . (1974) :

$$NDVI = \frac{r_5-r_4}{r_5+r_4} \quad (16)$$

The longwave radiation emitted by the atmosphere toward the surface $R_{ol,atm}$(W m $^{-2}$) was calculated via the Stefan–Boltzmann equation (Equation 17):

$$R_{ol,atm} = \varepsilon_a \sigma T_a^4 \quad (17)$$

where σ is the Stefan–Boltzmann constant; T_a is the surface air temperature (K); and ε_a is the atmospheric emissivity, obtained according to Duarte, Dias and Maggiotto (2006) (Equation 18):

$$\varepsilon_a = 0{,}625\,.\left(\frac{e_a}{T_a}\right)^{0{,}13} \quad (18)$$

E m where e_a is the vapor pressure (Pa) and e T_a is the surface air temperature (K).

The comparative analysis was performed by calculating the absolute errors (EAs) and relative errors (ERs) of the estimated Rn data according to Equations 19 (EA) and 20 (ER):

$$EA = |Rn_o * Rn_e| \quad (19)$$

$$ER = \frac{|Rn_o * Rn_e|}{Rn_o} * 100\% \quad (20)$$

where Rn_o represents the information observed in the field (coinciding with the time of the satellite passage) at the micrometeorological tower and where Rn_e represents the information estimated by the SEBAL model.

5 RESULTS AND DISCUSSION

5.1 Meteorological variables of the region

Figure 4 presents the average data collected by the sensors installed in the tower, which refer to the meteorological variables: air temperature (Tar), relative humidity (RH) and precipitation (PP) for the period from January 2018 to December 2019, as well as the average data of the climatological normal (NC) for the same variables (Tar-NC, RH-NC and PP-NC, respectively). In the period between January and May, the highest levels of precipitation (PP) and relative humidity (RH) and the lowest average air temperature (Tar) are

observed, whereas in the period between August and November, the lowest accumulated precipitation (PP) and highest average Tar are observed. When comparing the values obtained in the tower with the climatological normal (whose focus is the identification of the average value of a climatic variable in a delimited period), it is possible to notice a pattern similar to that presented in the graph plotted with the data of the present study, verifying that for RH, there was a greater difference (7.3%), whereas in relation to Tar, the values obtained in the field were lower in the months of January to May and December and higher from June to November. The precipitation (PP) data revealed that February was the month with the highest average rainfall, and this month presented a 148 mm difference from the climatological normal.

Figure 4(a) Average monthly air temperature and monthly relative humidity (collected by sensors in the tower and climatological normal-NC) and (b) average total monthly precipitation in the period from 2018--2019**.**

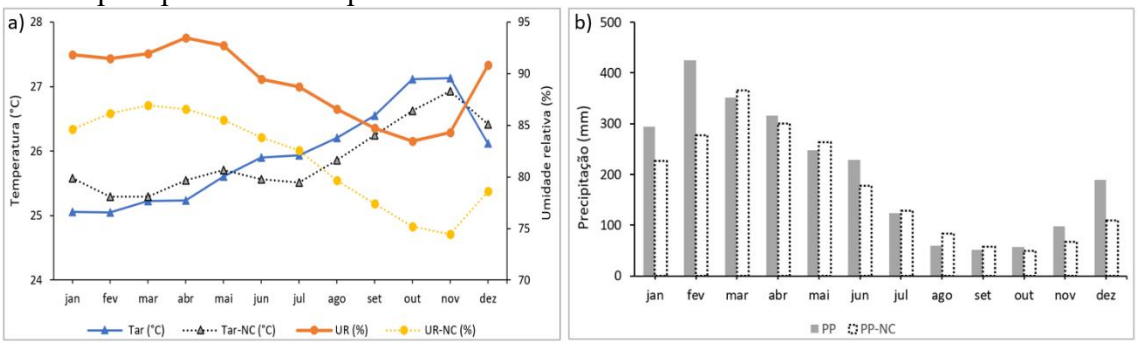

Source: Denis Pinho de Sousa (2019).

The data obtained corroborate the climatic characterization of Capitão Poço by Pacheco and Bastos (2001), in which the authors define four distinct periods during the year for the municipality: the rainy period (December--May), dry period (October), dry period (July --September) and transition period (June--November).

5.2 Surface temperature (TS) and net radiation (R_n)

TS is essential within SEBAL, as it is computed from the values of longwave radiation emitted by the surface (Equation 11). In the analyzed scene, regarding the surface temperature (TS) for day 151/2018, within the rainiest period in the region, an estimated average of 25.39 °C was obtained (with a maximum of 27.47 °C and a minimum of 21.28 °C). For day 241/2019, within the period in which PP accumulations decreased and the region's Tar averages began to rise, the estimated average was 27.2 °C (with a maximum of 34.21 °C and a minimum of 21.30 °C). In Figure 5, the highest TS records (in yellow, orange, and red) are located in areas designated for agriculture and in areas of exposed soil, where values above 30 °C are reached. The lowest TS values observed are mainly in regions covered by dense vegetation and secondary vegetation, water bodies and clouds, with average temperatures of approximately 20 °C recorded at these points.

Figure 5 Surface temperature (TS) estimated via SEBAL. (5.a) Day 151/2018; (5.b) day 241/2019**.**

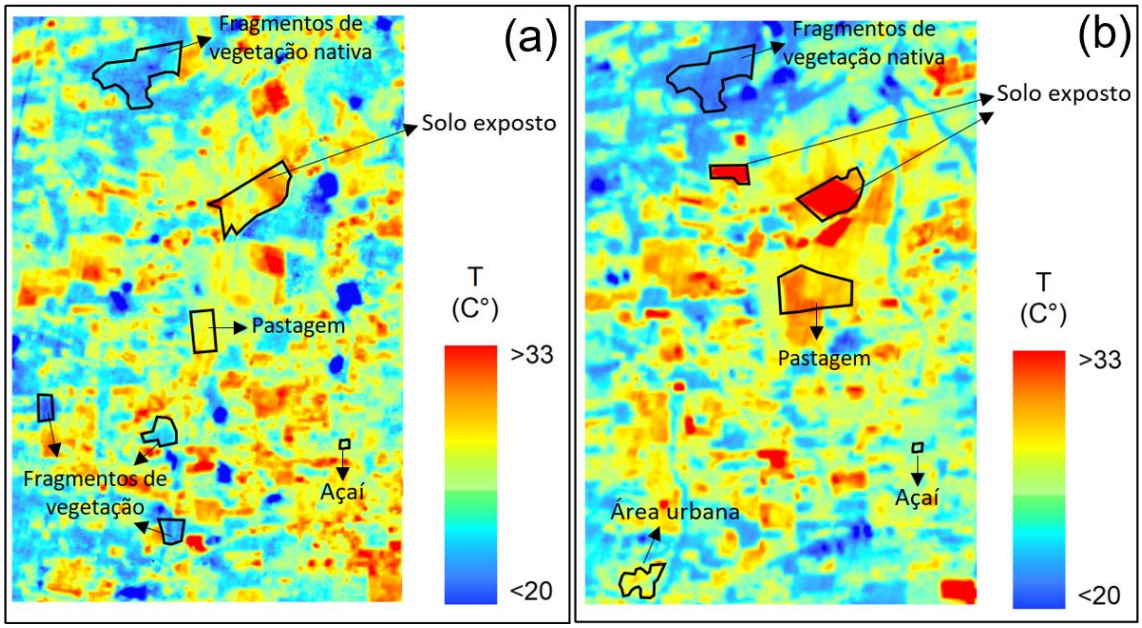

Source: Authors (2021).

The results obtained for TS in this study corroborate the research carried out by Crispim *et al*. (2020) in Santa Luzia do Pará, a municipality bordering Capitão Poço, belonging to the same mesoregion, in which the authors, when using remote sensing, identified an increase in TS in areas of exposed soil, recorded temperatures above 29 °C and a decrease in TS values in areas with dense vegetation, clouds and water bodies, where they obtained values below 22 °C.

Figure 6 shows the spatial distribution of surface temperature, estimated via SEBAL, in the açai plantation plot, which presented an overall scene average of 26.39 °C. For DSA 151/2018, the maximum temperature was 25.72 °C, and the minimum temperature was 25 °C. This period (the period corresponding to the scene) is considered the rainiest period in the region, as shown in Figure 4.b, which shows the average total monthly precipitation. For DSA 241/2019, the maximum temperature was 27.75 °C, and the minimum temperature was 26.10 °C, in accordance with the dry period (July --September), characterized by Pacheco and Bastos (2001) in their studies in Capitão Poço.

Figure 6 Surface temperature estimated via SEBAL in the açai plantation. On (a) day 151/2018 and (b) day 241/2019.

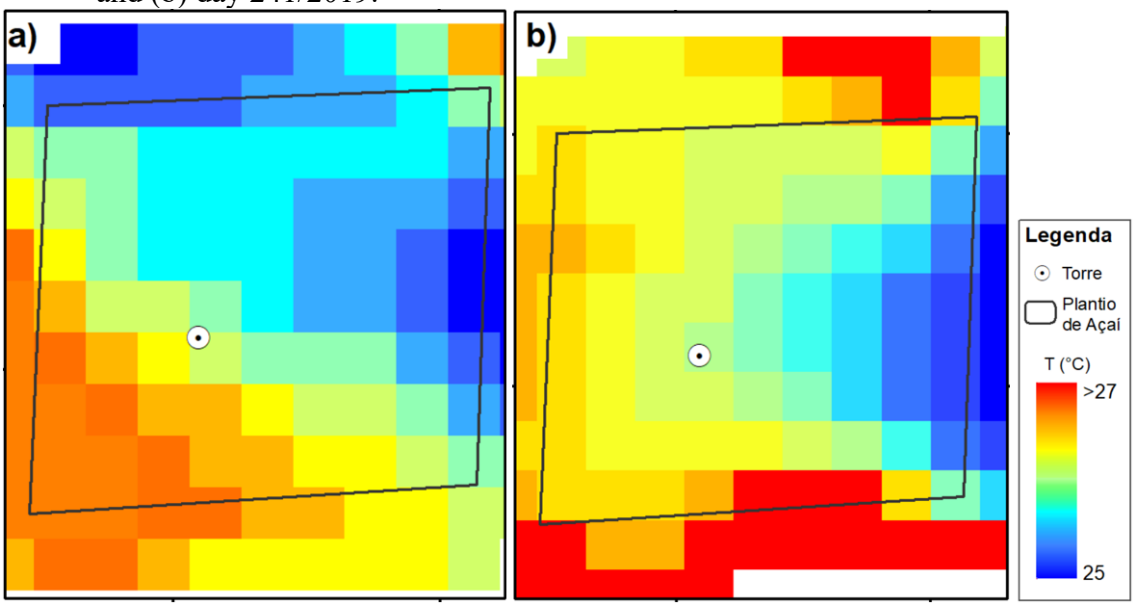

Source: Authors (2021).

In the analyzed scene, in relation to R_n, an average of 575.10 W/m² was recorded for day 151/2018, and 623.85 W/m² was recorded for day 241/2019. In Figure 7, the distribution of the estimated values of R_n at the surface is observed, and there is an oscillation of values below 200 W/m² (in green, values referring to clouds in the image) and values on the order of 700 W/m² (in red). The $R_{n\ peaks}$ were recorded in areas of forest and secondary vegetation, according to Jensen (2015), which occurred because these areas have a high leaf area index, and the soil is well supplied with water, which causes the temperature to decrease, also decreasing the emission of long waves, which consequently increases R_n. R_n peaks were also recorded in areas with water bodies, as water has low reflectance, thus causing greater energy absorption (PEREIRA *et al*., 2007).

Figure 7 Distribution of R_n estimated via SEBAL. (**a**) Day 151/2018, (b) day 241/2019.

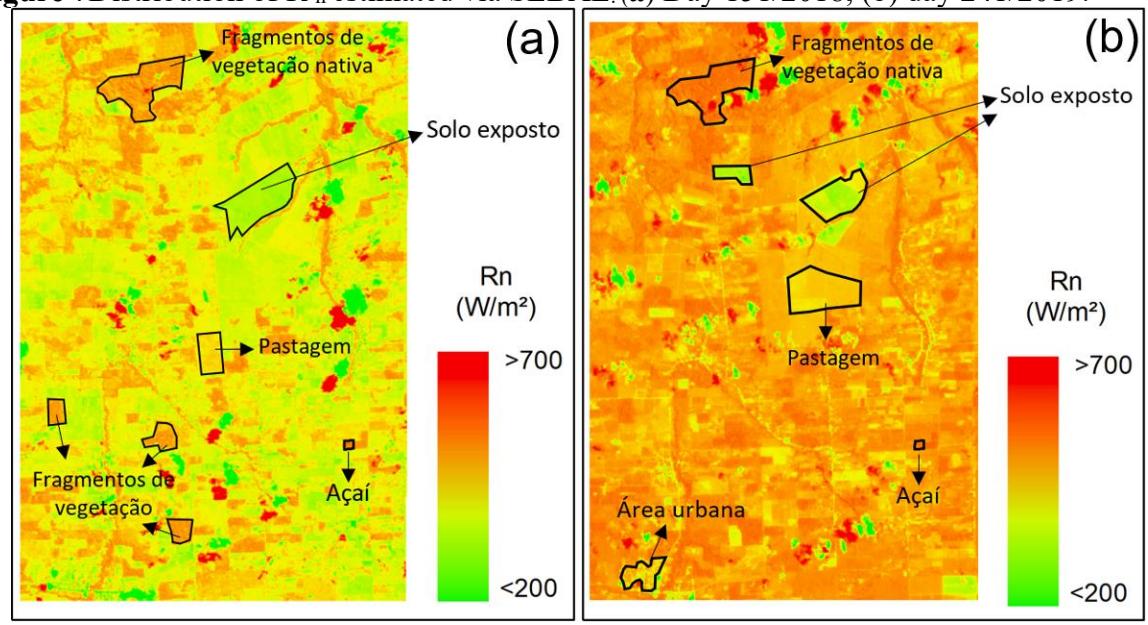

Source: Authors (2021).

The lowest values were recorded in modified areas, such as exposed soil and those designated for agricultural activities, as in these areas, there is a smaller amount of energy stored on the surface due to the smaller amount of vegetation cover and, according to Asner *et al*. (2000), under these conditions, the influence of the leaf component on the spectral response is reduced. Other studies have reported lower $R_{n\ values}$ in areas with low or no vegetation cover (GOMES *et al*., 2009; SANTOS; NASCIMENTO; RAO, 2011). Thus, the radiation balance follows a decreasing trend as the transition from an area of vegetation to one with exposed soil occurs.

The trend of decreasing estimated Rn values $_{in}$ the transition from areas of dense vegetation to areas of exposed soil was also verified in the study by Silva *et al*. (2015). In their analysis, this reduction was observed in accordance with the change in land cover, with higher averages observed in native Amazon forests and lower averages in pasture areas in southwestern Amazonia, largely due to the higher albedo of these covers (grass vegetation) compared with the pattern observed in forest regions. The variation in Rn during the rainy season (151/2018) in relation to the dry season (241/2019) increased by approximately 8% because even with little cloud cover, as observed in Figure 6.a, the atmosphere during this period of the year is more humid, contributing to greater absorption of incident shortwave radiation than what occurs during the drier period.

An approximate percentage was found by Rothmund *et al*. (2019) in the southern region of the Amazon rainforest, where the authors reported variations of 7% and 6% from the rainy to the dry season in forest and pasture areas, respectively. Studies by Pavão *et al*. (2016) and Santos *et al*. (2014), using SEBAL, also recorded a decrease in $R_{n\ values}$ as the scenes transitioned from Amazon rainforest areas to pasture regions.

Figure 8 shows the spatial distribution of R_n estimated with SEBAL in the açaí plantation plot, which presented a general average of 632.62 W/m². This value was lower than that reported in other studies carried out in the Amazon biome. Borella *et al*. (2018), analyzing Rn through SEBAL in irrigated agricultural areas (Cerrado–Amazon transition) south of the Amazon biome, obtained an average of 549.74 W/m².

De Oliveira *et al*. (2016), analyzing the radiation balance in the Amazon, in areas of native vegetation and pastures, in the southwest of the state of Pará, recorded an average R_n of 505.5 W/m². Notably, in the analysis carried out in this study, the lowest value observed within the plantation was 548.91 W/m² on 151/2018, and the highest value was 662.94 W/m² on 241/2019.

Figure 8 Distribution of R_n estimated by SEBAL in açaí planting. (a) Day 151/2018, (b) day 241/2019.

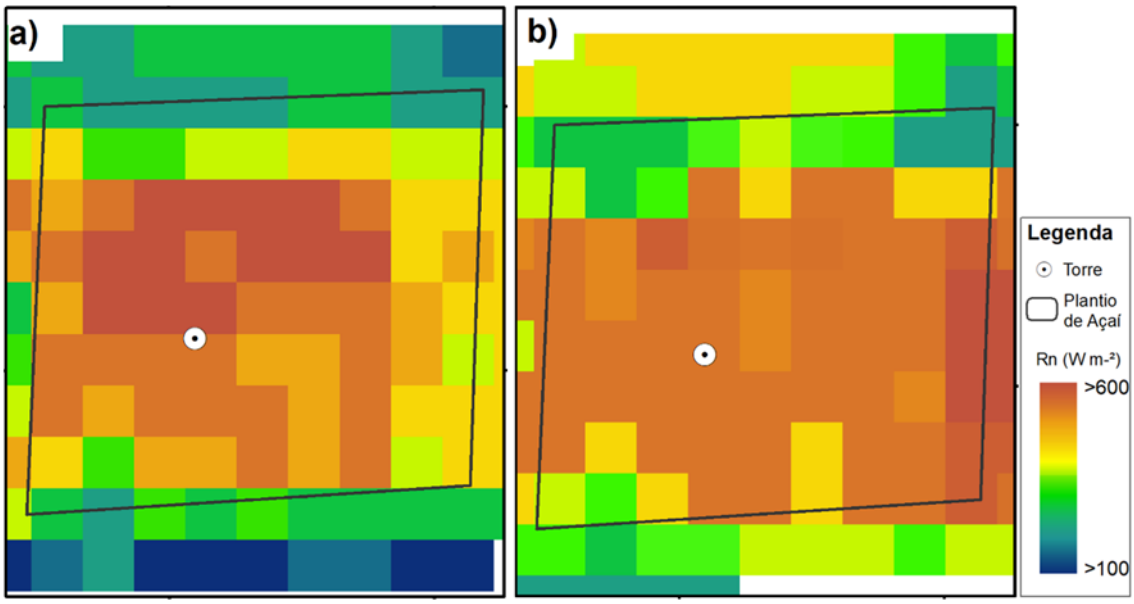

Source: Authors (2021).

In Figure 8, we can observe that there are different R_n values in the plot itself (for day 151/2018, the average, maximum and minimum values were 616.21 W/m², 633.67 W/m² and 548.91 W/m², respectively; for day 241/2019, these values were 648.59 W/m², 662.94 W/m² and 627.52 W/m², respectively), which are being directed to different processes (PICCOLO, 2019), since the energy available in the environment can be distributed for heating the air and soil as well as for plant transpiration processes (BIUDES *et al*., 2015), which demonstrates the importance of considering the spatial variability existing in the area for analyses in different studies, including R_n, which is another option to assist in decision-making regarding irrigation management.

Table 3 presents the average surface temperature (TS) estimated by the algorithm, the R_n values obtained at the micrometeorological station, the R_n values estimated by SEBAL for the location of the micrometeorological tower, and the relative (ER) and absolute (EA) errors of R_n for the two study dates.

Table 3. Surface temperature (TS) and R_n obtained by the micrometeorological tower sensors, R_n estimated via SEBAL, and the relative error (ER) and absolute error (EA) of the estimated R_n.

Julian Day	TS observed (°C)	R_n observed (W m-²)	R_n (W m-²)	ER (%)	EA (W m $^{-2}$)
151/2018	29.65	608.60	603.68	0.98	4.92
241/2019	30.15	647.10	631.44	3.4	15.66

Source: Authors (2021).

The errors observed in this study presented a good estimate and are in agreement with the literature on this subject, according to Daughtry *et al*. (1990), for studies involving measurements and estimates of Rn via multispectral remote sensing data and surface data recorded by an automatic meteorological station from Campbell Scientific, the errors are less than 7%. Santos *et al*. (2010) and Oliveira and Moraes (2013), using the methodology to obtain Rn via SEBAL, reported promising relative error results for this component. In their studies at the Jaru Biological Reserve (REBIO Jaru) and Rondônia, respectively, these authors reported errors ranging from 2% to 16%, both in the Legal Amazon. Studies involving net radiation estimates via SEBAL are still rare in the state of Pará; however, the use of this methodology can contribute to estimating Rn, since this is one way to obtain ecosystem responses to environmental conditions.

6 CONCLUSIONS

The values of R_n and TS, estimated by SEBAL, changed according to the modification of the landscape from dense forests to pasture areas and exposed soil and according to the season.

The results obtained from the use of the SEBAL algorithm for the $R_{n\ component}$ were satisfactory because the relative error was less than 7%, in accordance with the literature.

SEBAL was sensitive in differentiating the types of soil cover in the analyzed scene, as well as in the açai plantation itself, proving to be an effective tool that can be used to assist in decision-making regarding irrigation management.

7 ACKNOWLEDGMENTS

We would like to thank the Coordination for the Improvement of Higher Education Personnel - CAPES, for granting the first author a master's scholarship in the Postgraduate Program in Agronomy - PgAgro, the Federal Rural University of the Amazon - UFRA, the Federal University of Campina Grande - UFCG and the Soil Plant Atmosphere Interaction in the Amazon research group - ISPAAM, for providing the physical structure for the development of this work.

8 REFERENCES

ALLEN, RG TASUMI, M.; TREZZA, R. Satellite-Based Energy Balance for Mapping Evapotranspiration with Internalized Calibration (METRIC) - Applications. **Journal of Irrigation and Drainage Engineering** , New York, 133, no. 4, p. 395-406, 2007.

ALLEN, RG; TASUMI, M.; TREZZA, R. **SEBAL Surface Energy Balance Algorithms for Land: Advanced Training and Users Manual .** Version 1. Idaho. 2002. Available at: https://www.posmet.ufv.br/wp-content/uploads/2016/09/MET-479-Waters-et-al-SEBAL.pdf. Accessed on: 4 Aug. 2019

ALVARES, CA; STAPE, JL; SENTELHAS, PC; GONCALVES, JLM; SPAROVEK, G. Köppen's climate classification map for Brazil . **Meteorologische Zeitschrift** , Berlin, v. 22, n. 6, p. 711-728, 2013. DOI: https://doi.org/10.1127/0941-2948/2013/0507. Available at: http://143.107.18.37/material/mftandra2/ACA0225/Alvares_etal_Koppen_climate_classBrazil_MeteoZei_2014.pdf. Accessed on: September 3, 2020.

ALVES, LER; GOMES, HB; SANTOS, MN; FREITAS, IGF Radiation balance through the Landsat-8 satellite in the Pajeú River basin. **Journal of the Department of Geography** , São Paulo, v. 33, p. 117-127, 2017.

AN, N.; HEMMATI, S.; CUI, YJ. Assessment of the methods for determining net radiation at different time-scale of meteorological variables. **Journal of Rock Mechanics and Geotechnical Engineering** , [sl] , v. 9, no. 2 p. 239-246, 2017. Available at: https://www.sciencedirect.com/science/article/pii/S1674775516300944. Accessed on: 17 Jan. 2022.

ARAÚJO, WR; MEDEIROS, RM; FRANÇA, MV; HOLANDA, RM; PEREIRA, MLF; SABOYA, LMF Fluctuation of temperature and relative humidity in Recife–PE, Brazil. **Magazine Scientific Multidisciplinary** , Jundiaí , v. 2, n. 6, p. 26481, 2021 .

ASNER, GP; WESSMAN, CA; BATESON, CA; PRIVETTE, JL Impact of tissue, canopy, and landscape factors on the hyperspectral reflectance variability of arid ecosystems. **Remote Sensing of Environment** , New York, v. 74, no. 1, p. 69-84, 2000.

BASTIAANSSEN, WGM; MENENTI, M.; FEDDES, RA; HOLTSLAG, AAM A remote sensing surface energy balance algorithm for land (SEBAL) 1. Formulation. **Journal of Hydrology** , Amsterdam, vol. 213, p. 198-212, 1998.

BASTIAANSSEN, WGM; NOORDMAN, EJM; PELGRUM, H.; DAVIDS, G.; THORESON, BP; ALLEN, RG SEBAL Model with remotely sensed data to improve water-resources management under current field conditions. **Journal of Irrigation and Drainage Engineering** . New York, vol. 131, no. 1, p. 85-93, 2005.

BIUDES, MS; VOURLITIS, GL; MACHADO, NG; ARRUDA, PHZ; NEVES, GAR; LOBO, FA; NEALE, CMU; NOGUEIRA, JS Patterns of energy exchange for tropical ecosystems across a climate gradient in Mato Grosso, Brazil. **Agricultural and Forest Meteorology** . Amsterdam, vol. 202, no. 1, p. 112-124, 2015.

BORELLA, DR; SIQUEIRA, FRPS; FARIA, TO; BIUDES, MS; MACHADO, NG Effect of conversion of native vegetation into agricultural areas on biophysical variables in the Cerrado-Amazon transition region. **Ciência e Natura** , Santa Maria, v. 40, n. 1, p. e12, 2018.

CRISPIM, DL; BEZERRA, PES; LIMA, GVBA; PEREIRA, MM; FERNANDES, LL Analysis of vegetation index and surface temperature in the municipality of Santa Luzia do Pará, Amazon. **Journal of Hyperspectral Remote Sensing** , [sl], v. 10, no. 2, p. 77-86, 2020.

DAUGHTRY, C.S.T.; KUSTAS, W.P.; MORAN, MS; PINTER JR, PJ; JACKSON, R.D.; BROWN, PW; NICHOLS, W.D.; GAY, LW Spectral Estimates of Net Radiation and Soil Heat Flux. **Remote Sensing of Environment ,** Beltsville , vol. 32, p. 111-124. 1990.

DEBASTIANI, AB; SÁ, EA S; MARTINS NETO, RP; SCHIMALSKI, MB Mapping of the radiation balance in the São Joaquim National Park–SC. **Advances in Forestry Science** , Cuiabá , v. 5, n. 3, p. 363-367, 2018.

DE OLIVEIRA, G.; BRUNSELL, N.A.; MORAES, E.C.; BERTANI, G.; SANTOS, T.V.; SHIMABUKURO, Y.E.; ARAGÃO, L.E. Use of MODIS sensor images combined with reanalysis products to retrieve net radiation in Amazonia. **Sensors** , [sl] , v. 16, no. 7, p. 956-984, 2016.

DUARTE, HF; DIAS, NL; MAGGIOTTO, SR Assessing daytime downward longwave radiation estimates for clear and cloudy skies in Southern Brazil. **Agricultural and Forest Meteorology** , Amsterdam, vol. 139, no. 3-4, p. 171-181, 2006.

ENORÉ, DP **Studies of surface radiation balances estimated by satellites** . Dissertation (Master in Meteorology) – National Institute for Space Research, São José dos Campos, 2012.

FONTANA, DC; BERLATO, MA; BERGAMASCHI, H. Energy balance in irrigated and nonirrigated soybean. **Brazilian Agricultural Research** , [sl], v. 26, n. 03, p. 403-410, 1991.

GARRISON, J.D.; ADLER, GP Estimation of precipitable water over the United States for application to the division of solar radiation into its direct and diffuse components. **solarenergy** , [sl], v. 44, no. 4, p. 225-241, 1990.

GOMES, HB; SILVA, BB; CAVALCANTE, EP; ROCHA, HR Radiation balance in different biomes in the state of São Paulo using Landsat 5 images. **Geosciences** . Rio Claro, v. 28, n. 2, p. 153-164, 2009.

HUETE, A. A soil- adjusted vegetation index (SAVI). **Remote Sensing of Environment** . New York, vol. 25 , no. 3 , p. 295-309, 1988.

JENSEN, JR **Introductory Digital Image Processing** : **A Remote Sensing Perspective.** 4th Edition. University of South Carolina: Prentice Hall, 2015.
MACEDO, M.; DEFRIES, R.; MORTON, D.; STICKLER, C.; GALFORD, G.; SHIMABUKURO, Y. Decoupling of deforestation and soy production in the southern

Amazon during the late 2000s. **Proceedings of the National Academy of Sciences – PNAS** . New York . v. 109, no. 4, p.1341-1346. 2012.

MACHADO, CC; SILVA, BB; ALBUQUERQUE, MB; GALVINCIO, JD Energy balance estimation using TM - Landsat 5 images and the SEBAL algorithm on the southern coast of Pernambuco. **Brazilian Journal of Meteorology** , v. 29, n. 1, p. 55-67, 2014.

OLIVEIRA, G. de; MOAES, EC Validation of the radiation balance obtained from MODIS/TERRA data in the Amazon with LBA surface measurements. **Acta Amazônia** , Manaus, v. 43, n. 3, p.353-363, 2013.
PACHECO, NA; BASTOS, TX **Climatic characterization of the municipality of Capitão Poço-PA** . Belém: Embrapa Eastern Amazon , 2001.

PAVÃO, VM; NASSARDEN, DCS; PAVÃO, LL; MACHADO, NG; BIUDES, MS Impact of Conversion of Natural Cover into Pasture and Urban Area on Biophysical Variables in Southern Amazonas. **Brazilian Journal of Meteorology** , São José dos Campos, v. 32, n. 3, p. 343-351, 2017.

PAVÃO, VM; QUERINO, CAS; BENEDITTI, CA; PAVÃO, LL; QUERINO, JKAS, MACHADO, NG; BIUDES, MS Spatial and temporal variation of the net surface radiation in an area of southern Amazonas, Brazil. **Ra'ega Journal** , Curitiba, v. 37, n. 2, p. 333-352, 2016.

PEREIRA, G.; MORAES, EC; ARAI, E.; OLIVEIRA, LGL Preliminary study of the estimation of reflectance and albedo of Pantanal microsystems from satellite images. **Brazilian Journal of Cartography** , Rio de Janeiro, v. 59, n. 1, p. 55-61, 2007.

PICCOLO, MC Methods to estimate heat balance in coastal wetlands. *In* : PERILLO, G. ME; WOLANSKI, E.; CAHOON, DR; HOPKINSON, CS **Coastal Wetlands** . Second Edition. Amsterdam: Elsevier, 2019. Chapter 7, p. 263-288.

PINTO, LIC; COSTA, MH; DINIZ, LMF; SEDYAMA, GC; PRUSKI, FF Comparison of incident solar radiation products at the surface for South America. **Brazilian Journal of Meteorology** , São José dos Campos, v. 25, n. 4, p. 469-478, 2010.

RANA, G.; KATERJI, N. Measurement and estimation of current evapotranspiration in the field under Mediterranean climate : a review . **European Journal of Agronomy** , [sl], v. 13, no. 2-3, p. 125-153, 2000.

RODRIGUES, RSS; FERNANDES, LL; CRISPIM, DL; VIERIRA, ASA; PESSOA, CLL Morphometric characterization of the Igarapé da Prata watershed, Capitão Poço, Pará, Brazil. 11, n. 3, p. 143-150, 2016 **.**

ROTHMUND, LD; ALMEI DA JUNIOR, ES; LIMA, LPA; MASSAD, HAB; PALÁCIOS, RS; BIUDES, MS; MACHADO, NG; NOGUEIRA, JS Impact of land cover change on biophysical parameters in the southern Amazon rainforest by remote sensing. **Brazilian Journal of Climatology** , [sl], v. 25, n. 2, p. 122-137, 2019.

ROUSE, J.W.J.; HAAS, RH, SCHELL, JA, DEERING, DW Monitoring vegetation systems in the Great Plains with ERTS. **NASA special publication** , Washington, v. 351, no. 1974, p. 309-317 , 1974.

SANTOS, CACD; BEZERRA, BG; SILVA, BBD; RAO, TVR Assessment of daily actual evapotranspiration with SEBAL and S-SEBI algorithms in cotton crop. **Brazilian Journal of Meteorology** . São José dos Campos , v. 25, n. 3, p. 383-392. 2010.

SANTOS, CAC dos; WANDERLEY, RLN; ARAUJO, AL; BEZERRA, BG Obtaining the radiation balance in pasture and forest areas in the Amazon (dry season) using the MODIS sensor. **Brazilian Journal of Meteorology** . São José dos Campos , vol.29, n.3, p.420-432. 2014.

SANTOS, CAC; NASCIMENTO, RL; RAO, TVR Net radiation estimation under pasture and forest in Rondônia , Brazil, with TM Landsat 5 images. **Atmósfera** , Ciudad de México, v. 24, n. 4, p. 435-446, 2011.

SILVA, BB; BRAGA, AC; BRAGA, CC Radiation balance in the irrigated perimeter of São Gonçalo – PB using orbital images. **Caatinga Magazine** , Mossoró, v. 24 , n. 3, p . 145-152, 2011.

SILVA, BB; BRAGA, AC; BRAGA, CC; OLIVEIRA, LMM; MONTENEGRO, SMGL; BARBOSA JUNIOR, B. Procedures for calculation of the albedo with OLI- Landsat 8 images : Application to the Brazilian semiarid . **Brazilian Journal of Agricultural and Environmental Engineering** , Campina Grande , v. 20, n. 1, p. 3-8, 2016.

SILVA, LC; CUNHA, JM; MACHADO, NG; CAMPOS, MCC; BIUDES, MS Estimation of the radiation balance by remote sensing of different land uses in the southwestern Brazilian Amazon. **Sociedade & natureza** , Uberlândia, v. 27, n. 2, p. 341-356, 2015.

SOUZA, AP; ESCOBEDO, JF Estimates of global radiation incident on inclined surfaces based on the insolation ratio. **Brazilian Journal of Agricultural Sciences** , [sl] , v. 8, n. 3, p. 483-491, 2013.

STARKS, PJ; NORMAN, JM; BLAD, BL; WALTER-SHEA, EA; WALTHALL, CL Estimation of shortwave hemispherical reflectance (albedo) from bidirectionally reflected radiance data. **Remote Sensing of Environment** . New York , vol. 38, no. 2, p . 123-134, 1991.

TASUMI, M.; ALLEN, RG; TREZZA, R. At-surface reflectance and albedo from satellite for operational calculation of land surface energy balance. **Journal of Hydrologic Engineering** , Reston, vol . 13, no. 2, p. 51-63, 2008.

VELOSO, GA; SILVA, LAP; FERREIRA, ME Analysis of the radiation and energy balance in veredas areas in the North of Minas Gerais, cerrado biome. **Cerrados Magazine** , Brasília, v. 18, n. 1, p. 220-247, 2020.

ZHONG, Q.; LI, Y. Satellite Observation of surface albedo over the Quinghai -Xizang plateau region. **Advances in Atmospheric Sciences** , [sl], v. 5, no. 1, p. 57-65, 1988.